

<https://doi.org/10.1038/s41612-024-00636-y>

Dryland hydroclimatic response to large tropical volcanic eruptions during the last millennium

Check for updates

Shangrong Zhou¹, Fei Liu¹✉, Aiguo Dai²✉ & Tianbao Zhao³

Drylands are highly vulnerable to climate change due to their fragile ecosystems and limited ability to adapt. In contrast to the global drying after tropical volcanic eruptions shown previously, we demonstrate that large tropical volcanic eruptions can induce significant two-year hydroclimatic wetting over drylands by employing the last millennium simulations. During this wetting period, which extends from the first to the third boreal winter after the eruption, several hydroclimatic indicators, such as self-calibrating Palmer Drought Severity Index based on the Penman-Monteith equation for potential evapotranspiration (scPDSI_{pm}), standard precipitation evapotranspiration index (SPEI), aridity index (AI), top-10cm soil moisture (SM_{10cm}), and leaf area index (LAI), show significant positive anomalies over most drylands. The primary contribution to the wetting response is the potential evapotranspiration (PET) reduction resulting from dryland surface cooling and reduced solar radiation, as well as a weak contribution from increased precipitation. The latter is due to the wind convergence into drylands caused by slower tropical cooling compared to drylands. The wetting response of drylands to volcanic eruptions also demonstrates some benefits over the global hydrological slowdown resulting from stratospheric aerosol injection, which replicates the cooling effects of volcanic eruptions to address global warming.

Drylands are typically defined as regions where climatological annual precipitation (P) is well below the annual potential evapotranspiration (PET)^{1,2}. They are mainly located in subtropical regions in Africa, Asia, Australia, and the Americas²⁻⁶. Drylands cover approximately 41% of the Earth's land surface^{2,7} and sustain over 38% of the world's population^{7,8}. Furthermore, 90% of the countries over drylands are developing countries that are vulnerable to climate resilience^{7,8}. Drylands play a crucial role in global ecosystems, as they contribute around 40% of the Earth's net primary productivity^{9,10} and are home to about 30% of the world's endangered species¹¹. Due to their fragile ecosystems, combined with limited socio-economic adaptation and mitigation capacity, drylands are highly vulnerable to the impacts of climate change^{2,12}. Understanding dryland hydroclimatic variations and improving our ability to predict hydroclimatic variabilities have always been important priorities for scientific communities¹³⁻¹⁸.

Dryland hydroclimatic variations mainly include P, runoff, soil moisture, and drought changes, and they show a drying response to global warming during the recent decades in observations and climate models, which can be attributed to internal variability and external forcing, such as human activities¹⁶⁻²⁵. Volcanic eruptions, a significant natural external forcing, have been found to cause a significant decrease in global land-averaged P lasting for 2–3 years after the eruptions²⁶⁻³⁰. Volcanic eruptions can inject large amounts of sulfur gas, which forms sulfate aerosols in the stratosphere²⁸. These aerosols can reflect sunlight, resulting in surface cooling and a slowdown of the hydrological cycle^{28,30} due to reduced incoming shortwave radiation³¹. After tropical volcanic eruptions, however, positive P anomalies were observed over most drylands except for Africa, northern Australia, and the Middle East²⁹ and in model simulations except for parts of Australia controlled by the monsoon-desert coupling mechanism³². Positive runoff anomalies were also simulated over most

¹School of Atmospheric Sciences Sun Yat-Sen University, Key Laboratory of Tropical Atmosphere-Ocean System Ministry of Education, and Southern Marine Science and Engineering Guangdong Laboratory, Zhuhai 519082, China. ²Department of Atmospheric and Environmental Sciences, University at Albany, State University of New York, Albany, NY 12222, USA. ³Key Laboratory of Regional Climate-Environment Research for Temperate East Asia, Institute of Atmospheric Physics (IAP), Chinese Academy of Sciences (CAS), 100029 Beijing, China. ✉e-mail: liufei26@mail.sysu.edu.cn; adai@albany.edu

dryland regions³² and observed over southern North America and southern South America^{29,33}. These positive anomalies, however, are relatively small.

Hydroclimatic variations can occur for both the supply and demand of land surface water, which are typically represented by P and PET, respectively. The self-calibrating Palmer Drought Severity Index based on the Penman-Monteith equation for PET (scPDSIpm)³³ incorporates both antecedent and current water supply (P) and demand (PET) to quantify the cumulative departure of surface water balance³⁴. By considering these factors, it has been widely used in analyzing hydroclimatic variations over global land^{21,29,35,36}. From the perspective of water balance, it remains uncertain whether the weak positive increase in dryland P following tropical eruptions, as indicated by previous study³², will lead to significant hydroclimatic responses in drylands. After the mean of five years before the eruptions was used as the reference to remove most of the internal variations, the wetting response and positive scPDSIpm anomalies were observed in most drylands within one year following the 1991 Mount Pinatubo eruption, except for South Africa and certain regions of Australia²⁹. However, it is still unclear whether such a response is representative of other tropical eruptions, as a multi-eruption composite is needed to eliminate internal variations.

The proposal to inject sulfur aerosols into the stratosphere as a method to mitigate global warming by mimicking the cooling effect of volcanic eruptions has led to the suggestion that this may result in a wetting response, characterized by an increase in the ratio of P and PET, over drylands in North America and South America³⁷. In the last millennium simulations of the Community Earth System Model (CESM), positive anomalies seem to appear in scPDSIpm over southern North America and southern South America, as well as in soil moisture in certain dryland regions within two years after tropical volcanic eruptions^{38,39}, although these studies did not specially focus on drylands. Furthermore, previous studies have only shown wetting responses from some certain of surface water supply or demand, not surface water balance. The wetting signal, as indicated by various

hydroclimate indicators, has been observed or simulated over drylands following a global hydrological cycle slowdown after tropical eruptions or stratospheric sulfur aerosol injections. This has prompted further investigation into the hydroclimatic response of drylands to tropical volcanic eruptions.

In this study, we investigate the hydroclimatic response in global drylands to large tropical volcanic eruptions. We analyze the Last Millennium simulations from 10 climate models that participated in the Paleoclimate Modeling Inter-comparison Projects (PMIPs) and the CESM Last Millennium Ensemble (CESM-LME) full forcing simulations. Additionally, we compare these findings with the hydroclimatic responses in the last millennium reconstructions and observation-derived data (see Methods for details).

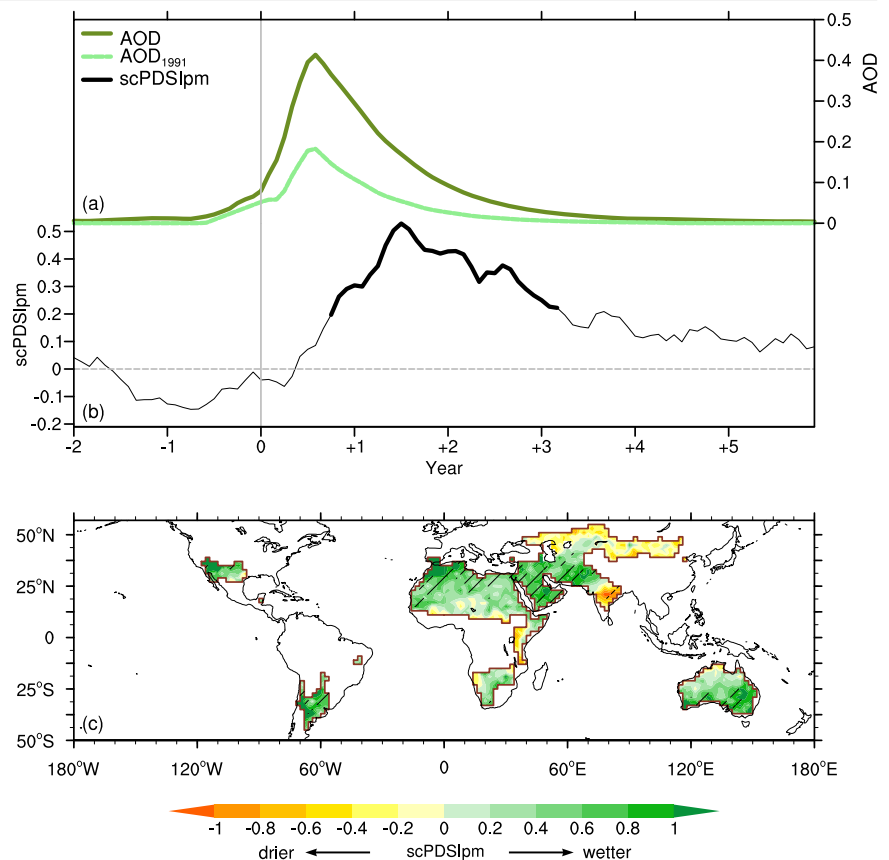
Results

Simulated dryland wetting response to large tropical volcanic eruptions

The multi-model ensemble mean (MME) of the climatological aridity index (AI) from 11 Last Millennium (LM) simulations (see Methods) is used to define the climatic drylands with $AI < 0.65^1$ (Supplementary Fig. 1a). The simulated drylands, which closely match the observed patterns (Supplementary Fig. 1b)^{2,6,15}, are primarily located in subtropical regions, including southern North America, southern South America, northern and southern Africa, the Middle East, and Australia.

After tropical volcanic eruptions, the mean aerosol optical depth (AOD) derived from 114 selected eruptions in 11 LM simulations during 850–1850 AD (see Methods) shows an increasing trend. The average AOD reaches its peak of about 0.4 (for comparison, the average AOD of the 1991 Mount Pinatubo eruption is 0.18) in the middle of the eruption year (Fig. 1a). In PMIPs, the eruption season is not considered, and the volcanic aerosol is typically assumed to reach its peak during the middle of the year⁴⁰. The MME of scPDSIpm, when averaged over global drylands, exhibits a positive anomaly (up to 0.5) lasting for more than five years after the

Fig. 1 | Simulated global dryland scPDSIpm response to large tropical volcanic eruptions.
a MME of the globally averaged monthly AOD before and after the selected tropical eruptions larger than the Mount of Pinatubo eruption in 1991 (see Methods) during the period 850–1850 AD for all 11 models (dark green line), as well as the Mount of Pinatubo eruption in 1991 (light green line), with zero on the x-axis denoting the eruption time.
b Composite of three-month running mean of dryland scPDSIpm anomalies relative to the five-year mean preceding the selected tropical eruptions. Changes significant at the 5% level are in bolded. “0” on the x-axis represents the start of the eruption year (Year0), and “+1/–1” represents the start of the first year after (Year1)/before (Year-1) the eruption. The monthly scPDSIpm was calculated using model data following Dai²¹.
c Composite of scPDSIpm anomalies averaged from November of Year0 to March of Year3 for eruptions. Brown contours are used to outline the drylands. Changes significant at the 5% level are hatched.



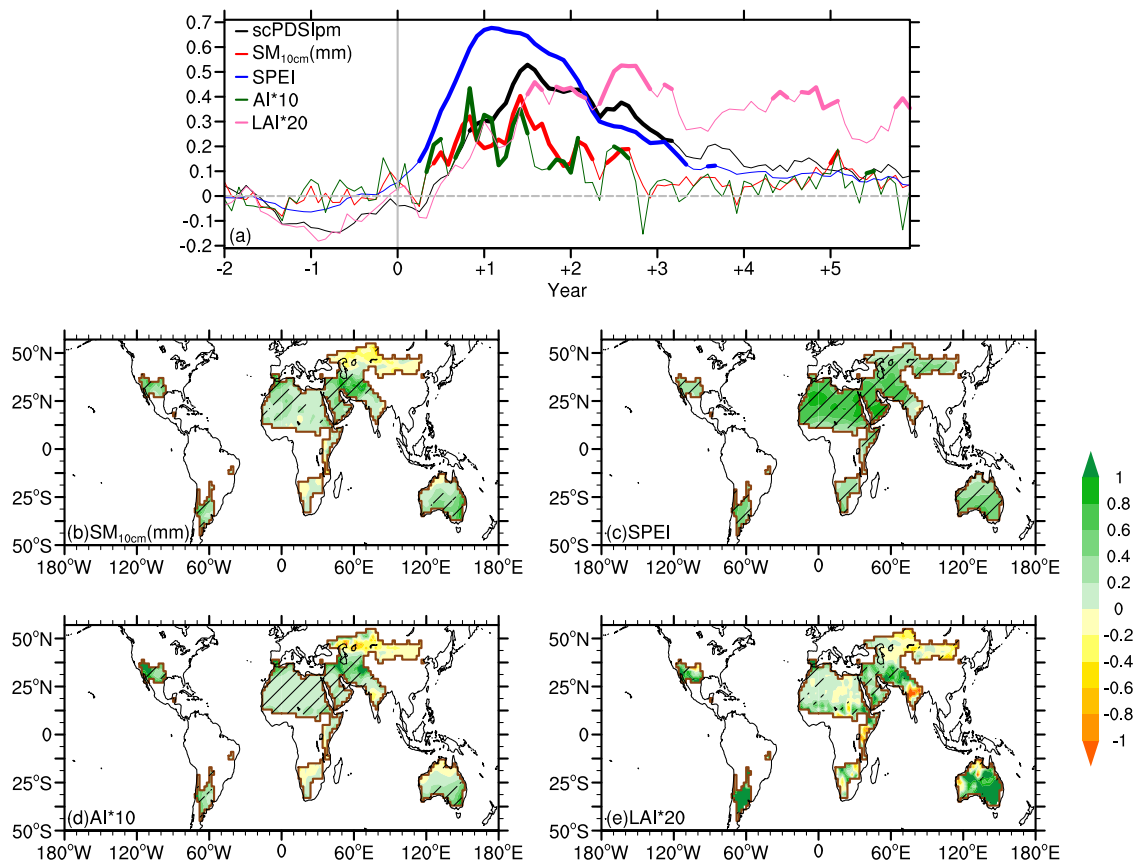


Fig. 2 | Simulated global dryland SM_{10cm} , SPEI, AI, and LAI responses to large tropical volcanic eruptions. **a** Composite of three-month running mean of dryland SM_{10cm} (red line), SPEI (blue line), AI (multiplied by 10 for comparison, green line), LAI (multiplied by 20 for comparison, pink line), and scPDSIpm anomalies (black line) relative to the five-year mean preceding the eruptions during the period 850–1850 AD from 11 model simulations. Changes significant at the 5% confidence

level are bolded. “0” on the x-axis represents the start of the eruption year (Year0), and “+1/–1” represents the start of the first year after (Year1)/before (Year–1) the eruption. Composite anomalies of **(b)** SM_{10cm} , **(c)** SPEI, **(d)** AI, and **(e)** LAI averaged from November of Year0 to March of Year3 for the selected eruptions. Brown contours are used to outline the drylands. Changes significant at the 5% level are hatched.

eruptions (Fig. 1b). This significant anomaly in the scPDSIpm can be found from November of the eruption year (Year0) to March of the third year after the eruption year (Year3). The largest positive anomaly, reaching a value of 0.53, occurs in July of Year1, approximately one year after the peak AOD.

In addition to scPDSIpm, we also examined other hydroclimatic responses, such as SM_{10cm} , SPEI, AI, and LAI. Significant positive anomalies are simulated for SM_{10cm} , SPEI, AI, and LAI, lasting for three to four years following the eruption (Fig. 2a). The largest positive anomalies, with values of 0.4 for SM_{10cm} , 0.7 for SPEI, 0.04 for AI, and 0.03 for LAI, are simulated, and these amplitudes are comparable to their respective interannual variations. When considering only the current surface water supply and demand but neglecting the cumulative water budget, both the SPEI and AI exhibit significant positive anomalies, typically occurring a few months before the anomalies seen in the scPDSIpm.

During the wetting period from November of Year0 to March of Year3, significant positive scPDSIpm anomalies are simulated over most global drylands, with the exception of parts of northern Central Asia, India, and a few other areas (Fig. 1c). Previous studies have identified a drying anomaly in India related to decreased summer monsoon P after tropical volcanic eruptions⁴¹. The largest wetting response can be found over the Middle East, where scPDSIpm anomaly exceeds 2 (for comparison, PDSI < –2.0 is considered as moderate to severe drought¹⁹). The amplitude of the scPDSIpm response to large tropical volcanic eruptions is comparable to its interannual variations, which can be measured by the standard deviation of the annual scPDSIpm over drylands, with a value of about 1.0. Furthermore, the simulated SM_{10cm} , LAI, SPEI, and AI also show positive anomalies over most drylands (Fig. 2b–e).

The wetting response is also simulated for individual volcanic forcings (Supplementary Fig. 2). Additionally, the means of 9 ensembles of GISS-E2-R and 12 ensembles of CESM-LME also demonstrate a similar wetting response over the drylands after eruptions (Supplementary Fig. 3). Although divergent responses are simulated for certain indices, such as negative anomalies in AI and LAI against positive SPEI and SM_{10cm} anomalies over India and northern Australia, the overall consistent responses across different hydroclimatic indices suggest that the wetting signal over drylands is a robust response to tropical volcanic eruptions.

Attributions of global dryland wetting response

After the eruptions, the averaged PET in global dryland drops quickly, reaching a peak decline of $-0.32 \text{ mm day}^{-1}$ in September of Year0; thereafter, PET begins to recover to climatology in Year4 after the eruption (Fig. 3a). The dryland P exhibits a weak reduction only in Year0, followed by a recovery and a slight increase beyond the climatology in Year 1 and Year 2. During Year0, the decrease in PET is much greater than the reduction in P, resulting in large increases in SPEI, AI, SM_{10cm} , and a delayed increase in scPDSIpm. After Year0, in addition to the positive contribution from the PET reduction, the weak increase in P from Year1 also partly contributes to the global dryland wetting response.

When keeping other variables unchanged after the eruptions, i.e., the same as the five-year mean preceding the eruption, the changes in PET due to those of surface air temperature (T) and surface net shortwave radiation (SW) are very close to all-factors-forced PET changes (Fig. 3a). This suggests that the response of dryland PET to tropical eruptions is mainly driven by the reductions in T and SW. The linear sum of PET changes due to each T

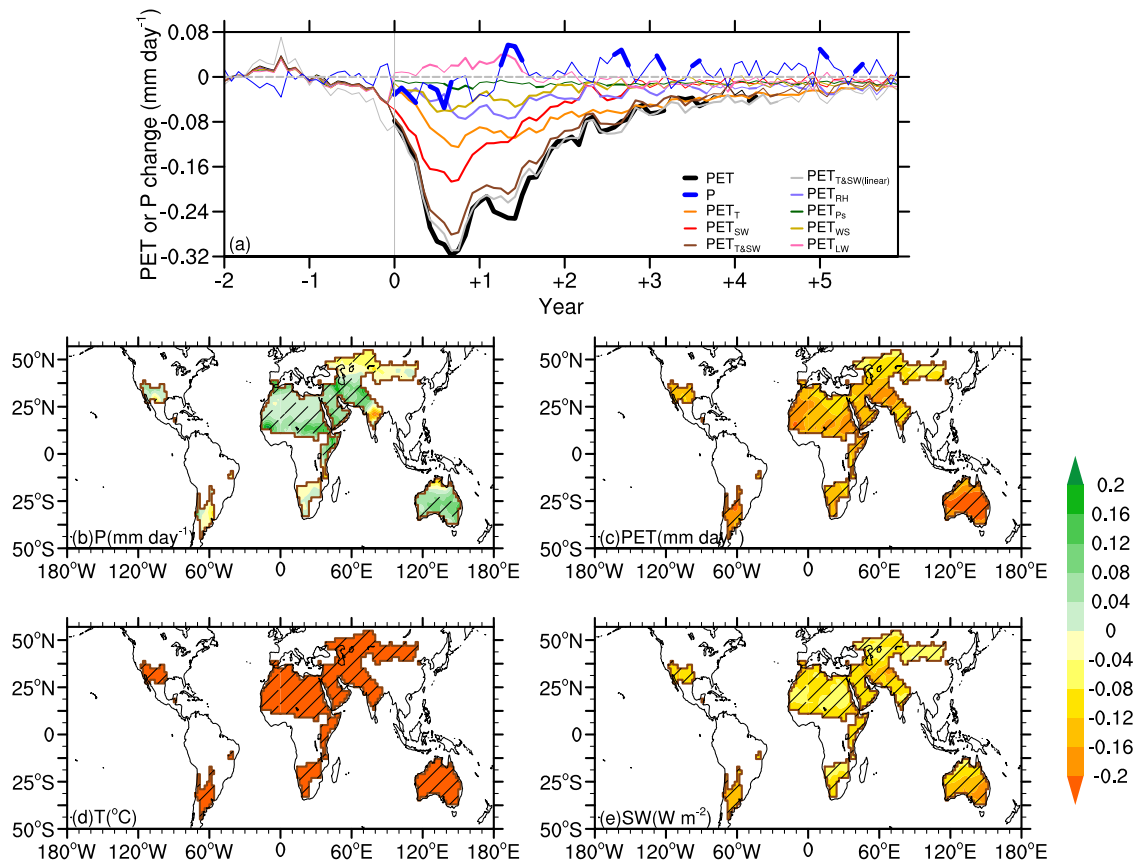


Fig. 3 | Attributions of global dryland wetting response after large tropical volcanic eruptions. **a** Composite of three-month running mean of global dryland PET changes forced by all factors (black line), a single variable or their different combinations (color lines, Supplementary Table 2), as well as P change (blue line), relative to the five-year mean preceding the eruptions in the LM simulations. Changes significant at the 5% confidence level are indicated by bold lines. “0” on the x-axis represents the start of the eruption year, and “+1–1” represents the start of

the first year after/before the eruption. Composite dryland anomalies, averaged for the significant wetting period from November of Year0 to March of Year3, are shown for **(b)** P (mm day⁻¹), **(c)** PET (mm day⁻¹) changes forced by all factors, **(d)** surface air temperature (T, °C), and **(e)** shortwave radiation (SW, W m⁻²) after the selected tropical eruptions. Brown contours are used to outline the drylands. Changes significant at the 5% level are hatched.

and SW change shows a smaller negative anomaly compared to the combined effect of these two variables. This indicates weak positive nonlinear feedback for the decrease in PET.

During the period of dryland wetting after volcanic eruptions, P also shows positive anomalies over drylands except for parts of southern North America, southern South America, South Africa, and northern Central Asia. The dryland-averaged anomaly is 0.039 mm day⁻¹ (Fig. 3b). However, PET displays a uniform decrease over global drylands, with a larger magnitude of -0.14 mm day⁻¹ (Fig. 3c), resulting from uniform decreases in both T and SW (Fig. 3d, e).

Over southern South America, southern Africa, and northern Central Asia, the reduction in PET, along with negative feedback from P reduction, contributes to wetting. Both PET reduction and P increase, however, contribute to the wetting over northern Africa, most of North America, Australia, and the Middle East. As for the AI index⁴², PET contributes much more to the wetting of drylands compared to P (see Supplementary Fig. 4).

Dryland P increases due to slower tropical cooling

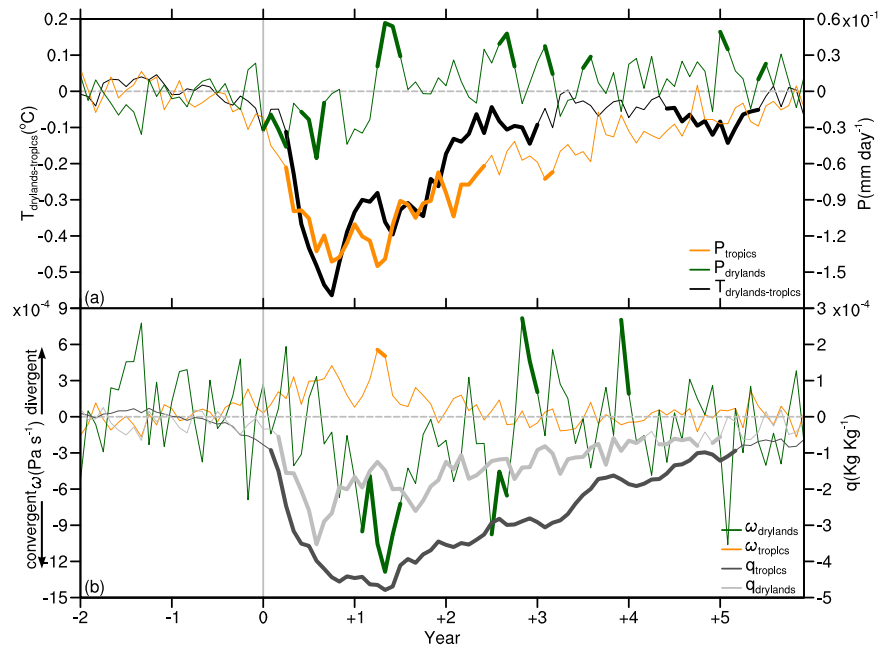
It is easy to understand that volcanic eruptions can reduce T and SW by reflecting incoming solar irradiance, while it remains puzzling as to why dryland P increases despite the surface cooling after Year0. As shown in Fig. 4a, dryland P initially experiences a negative anomaly during Year0, and then it becomes above normal starting from the spring of Year1, interrupted by periods with neutral anomalies. To explain this, we compared P anomalies between moist tropical regions (including both land and ocean) and drylands (Fig. 4a). There are two ways to change P: evaporation and

moisture convergence. The latter can be approximated by the vertical advection of lower-level moisture, which can be represented by the mid-troposphere vertical velocity at 500 hPa and the specific humidity at 925 hPa⁴³. Here a negative pressure velocity anomaly denotes upward motion in the atmosphere.

During Year0, the negative thermal contrast anomalies between drylands (primarily located in the subtropics, as shown in Supplementary Fig. 1) and the tropics reach their peak and play a dominant role in the change of dryland P (Fig. 4a). This leads to a decrease in dryland P, as winds converge towards the relatively warm tropical regions through the “Lindzen and Nigam mechanism”⁴⁴.

After Year0, the persistent negative thermal contrast anomalies between drylands and tropical regions (including both tropical land and ocean), along with negative moisture anomalies (Fig. 4b), cannot account for the increase in P over drylands. However, the negative dryland-tropical thermal contrast anomalies start to recover along with a downward motion anomaly (even if insignificant) over tropical regions. The negative moisture and P anomalies in the tropical regions reach their peak in Year1. Associated with this suppression of tropical convection, there will be a downward motion anomaly over the tropical regions, which will induce wind convergence towards the drylands through the “monsoon-desert coupling mechanism”^{45,46} and “weakened Hadley circulation mechanism”⁴⁷. These circulation anomalies can be observed in the lower troposphere (see Supplementary Fig. 5b). This convergence will cause an upward motion and an increase in P over drylands, despite moisture reduction there. If we take El Niño into account, increased convergence wind towards drylands and an

Fig. 4 | Tropical and dryland responses to large tropical volcanic eruptions. **a** Composite of three-month running mean of dryland-tropic thermal contrast anomalies ($^{\circ}\text{C}$, black line), as well as P anomalies (mm day^{-1}) over global drylands (green line) and tropical regions (orange line), with respect to the five-year average preceding the selected tropical volcanic eruptions in the LM simulations. The thermal contrast was defined by global dryland-averaged surface air temperature (T) minus tropic (20°S – 20°N)-averaged T . Anomalies significant at the 5% confidence level are represented by bold lines. “0” on the x-axis represents the start of the eruption year, and “+1/–1” represents the start of the first year after/before the eruption. **b** Same as **a**, but for 500 hPa vertical pressure velocity (ω , Pa s^{-1} , positive downward) over the drylands (green line) and tropical regions (orange line), as well as 925 hPa specific humidity (q , Kg Kg^{-1}) over the drylands (light gray line) and tropical regions (dark gray line).



upward motion anomaly contribute to a more wetting response of drylands (Supplementary Fig. 5c).

The delayed response of the ocean compared with the land after tropical eruptions has been demonstrated by previous studies^{27,41} since the ocean has a larger heat capacity than the land. Indeed, the delayed response also occurs over moist tropical regions compared to subtropical drylands, as the former has a larger capacity than the latter. This delayed tropical cooling can also be represented by the recovery of dryland-tropic thermal contrast after Year0. Thus, the tropical cooling will suppress evaporation and reduce tropical moisture and convection²⁵.

In summary, the main reason for the delayed reduction in P over the tropics is the slower cooling response compared to the drylands. This slower response results in wind converging towards the drylands and an increase in P there, which helps counteract the moisture deficiency after Year0. Although the dryland P increase is weak, our point is that there is no significant reduction in dryland during this period, so the significant reduction in PET will lead to significant wetting.

Reconstructed and observation-derived dryland wetting response

So far, we have utilized LM simulations to illustrate the two-year-wetting response of drylands to large tropical volcanic eruptions. It is currently unknown whether this simulated dryland wetting response can be observed in the reconstructions and historical data (see Methods). The average of two individual reconstructions, Paleo Hydrodynamics Data Assimilation product (PHYDA) and Last Millennium Reanalysis version 2 (LMR2), was taken into consideration. The reconstructed scPDSIpm over most drylands, with the exception of the Middle East, parts of southern South America and northern Africa, indicates a wetting response after the selected eruptions from 850 to 1850 AD. However, the amplitude of the response is relatively weak compared to the simulations, and a significant wetting response is only observed over the central Sahel (Fig. 5a). In the reconstructions, the internal variability of dryland scPDSIpm, as represented by the LM standard deviation, is approximately 0.5, which is half of the simulated response of 1.0. For each of these two reconstructions, similar spatial patterns are observed over most drylands, with differing responses noted over southern South America and western Australia (Supplementary Fig. 6).

For the three recent eruptions, namely the 1963 Agung, 1982 El Chichón, and 1991 Pinatubo eruptions, a wetting response can be found over most northern Africa and the Middle East for the 1963 Agung eruption; and

over southern South America, southern North America, and Australia for the 1982 El Chichón eruption. As for the 1991 Pinatubo eruption, most drylands show wetting responses, except for southern Africa, parts of Australia, and other regions (Fig. 5b–d). For individual events, using the five-year mean before the eruption as the baseline may not be able to remove all internal variations, which may differ before and after an eruption.

Discussion

Contrast to the global drying observed after tropical volcanic eruptions, our analysis of LM simulations exhibits a two-year hydroclimatic wetting response over drylands following these eruptions. The wetting response can be identified in different hydroclimatic indicators such as scPDSIpm, $\text{SM}_{10\text{cm}}$, SPEI, AI, and LAI, instead of solely focusing on the response of P ⁴⁸. The reduction in PET, resulting from surface cooling and reduced SW radiation over drylands, is large enough to induce substantial wetting of these regions after large tropical volcanic eruptions. Additionally, the weak increase in dryland P , unlike the strong reduction in P over tropical regions, also contributes partially to the wetting of drylands. The slower cooling response over the tropics relative to drylands leads to a delayed reduction in tropical P , which will cause wind convergence towards the drylands, increasing P and counteracting moisture deficiency after Year0 over drylands. Associated with this hydroclimatic wetting response following tropical volcanic eruptions, the increased soil moisture and greening LAI response over drylands show some benefits over the global hydrological slowdown for proposed geoengineering such as the stratospheric aerosol injection that can replicate the cooling effect of volcanic eruptions to address global warming^{48,49}. Indeed, these changes over drylands have also been identified in global crop fields, exhibiting an increasing trend under the stratospheric aerosol injection scenario⁵⁰.

The discrepancies between the reconstructed, observed responses and the simulated results, particularly in regions, such as Africa and the Middle East, warrant further investigation. Under different volcanic forcing datasets, the largest multi-model spread of scPDSIpm exceeds 0.25 (Supplementary Fig. 2b). The spread of other values can also be found in Supplementary Fig. 7. The selection of volcanic forcing dataset, the latitude of volcanic eruptions, the seasonality of volcanic eruptions, and the influence of El Niño–Southern Oscillation (ENSO)^{51–53} are potential factors. For example, the inclusion of El Niño was found to enhance the dryland wetting after tropical volcanic eruptions, with increased wind convergence towards to the

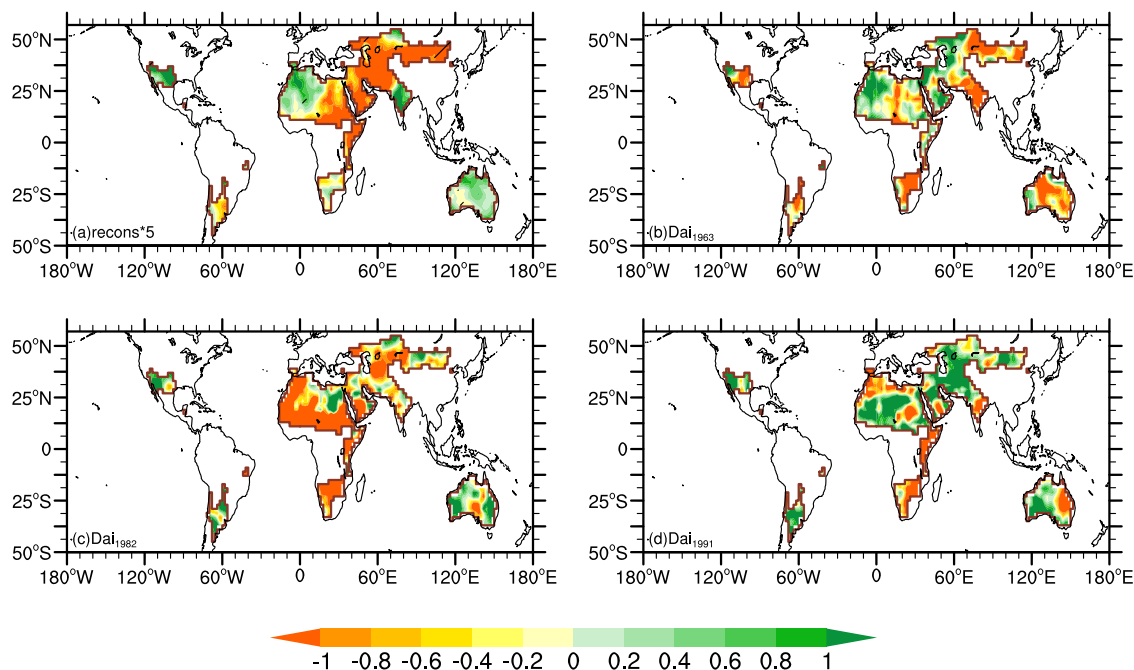


Fig. 5 | Reconstructed and observational scPDSIpm responses after large tropical volcanic eruptions. **a** Composite scPDSIpm anomalies relative to five-year average preceding the eruption, in the reconstructions (see Methods) for Year1-Year2 average after tropical volcanic eruptions from 850 to 1850 AD. Changes significant at

the 5% level are hatched. The Dai-scPDSIpm anomalies averaged from November of Year0 to March of Year3 after the **(b)** 1963 Agung, **(c)** 1982 El Chichón, and **(d)** 1991 Pinatubo eruptions.

drylands (Supplementary Fig. 5c). Thus, more attention should be devoted to minimizing the uncertainties among various datasets in the future.

Methods

Model data

We employed the LM simulations from 10 models participating in the Paleoclimate Modeling Inter-comparison Project Phase 3 (PMIP3)⁵⁴ and 4 (PMIP4)⁵⁵, as well as the CESM-LME⁵⁶, for the period of 850–1850 AD (Supplementary Table 1). The analyzed monthly variables and their abbreviations for these LM simulations are listed in Supplementary Table 2. Since most of the models only provided one ensemble run, we only used the first member run of CESM-LME simulations and the GISS-E2-R simulations to ensure that all models had the same weight in deriving the multi-model ensemble mean. The ensemble means of 12 CESM-LME ensembles and 9 GISS-E2-R ensembles were also investigated separately.

Four sets of reconstructed volcanic aerosol optical depth (AOD) were used to force the LM simulations, which were derived from Gao et al.⁵⁷ (GRA), Crowley, et al.⁵⁸ (CEA), Ammann, et al.⁵⁹ (AMM), and Toohey and Sigl⁶⁰ (TOO) (Supplementary Table 1). Only tropical eruptions (20°S–20°N) with intensity stronger than the 1991 Mount Pinatubo eruption were selected. The number of such strong tropical eruptions ranges from 9 to 12 during 850 to 1850 AD for each model (Supplementary Table 3). The LM simulations from 11 models were forced by these large eruptions, resulting in a total of 114 simulated eruption events. Noted that the 1991 referenced AOD was lacked in the TOO dataset, and was approximated by the ratio of 1815 Tambora between TOO and GRA datasets.

A volcanic eruption is considered to coincide with an El Niño when the averaged Niño3.4 index during the wetting period from the first to the third boreal winter after the eruption exceeds 0.5 standard deviation of the last millennium. The Niño3.4 index is defined as the area-averaged (5°S–5°N, 120°–170°W) sea surface temperature anomaly.

Reconstruction and observation-derived data

The response of scPDSIpm after tropical eruptions were analyzed by using the long-term reconstructions and observation-derived data based on the

Penman-Monteith equation for PET (Dai-scPDSIpm), respectively. The former was the average of two sets of annual mean reconstructed scPDSIpm, i.e., LMR2⁶¹ and PHYDA⁶² during the last 2000 years. The Dai-scPDSIpm is an observation-derived data over global land areas from 1850 to 2018 with a 2.5° grid resolution²⁰. To analyze scPDSIpm response reconstructed by the two datasets, the volcanic eruption date of Sigl et al.⁶³ was used, and there were a total of 22 tropical eruptions for the period of 850–1850 AD. As for Dai-scPDSIpm, focus was particularly put on three eruptions, i.e., the Mount Agung in 1963, the Mount El Chichón in 1982, and the Mount Pinatubo in 1991. The Global Aridity Index and Potential Evapotranspiration Database-Version 3 (Global_AI_PET_v3)⁶⁴ was also used to define the drylands in observation.

Composite and significance

Superposed epoch analysis (SEA⁶⁵) was employed to analyze the hydroclimatic responses to the selected large tropical volcanic eruptions. To isolate the climatic signals from the background noise, the climatological annual cycle of the five years preceding each eruption was removed for each eruption. An 11-year window spanning 5 years before and after each eruption was used for the SEA analysis. To avoid any single eruption from dominating the entire 11-year window, we also checked the effect of normalization within the window, and similar results were obtained (Supplementary Fig. 8). A significant test at the 5% confidence level was performed by randomly resampling the data 10,000 times to generate a probability density distribution, with an assumption that there was no correlation between volcanic eruptions and other climate variations⁶⁶.

Hydroclimatic indicators

We calculated five indicators, including scPDSIpm, SM_{10cm}, SPEI, AI, and LAI, to analyze the hydroclimatic response to large tropical volcanic eruptions. The scPDSIpm, SPEI, and AI indices represent the balance between land surface water demand and supply, and have been widely used in analyzing global aridity changes. Among them, SPEI and AI account for the current surface water balance, while scPDSIpm takes

precedent and current conditions into account. The scPDSIpm measures the cumulative departure in surface water balance⁶⁷. The SPEI represents climatic water balance that is calculated at different time scales⁶⁸. AI is measured by the ratio of annual P to PET⁶. Meanwhile, SM_{10cm} represents the water in land surface, and LAI represents the total leaf area per unit ground area⁶⁹. To calculate scPDSIpm, SPEI and AI, the PET is an important factor, which denotes atmospheric demand for water, and is calculated by the following equation⁷⁰:

$$PET = \frac{\Delta}{\Delta + \gamma} (R + A) + \frac{\gamma}{\Delta + \gamma} \frac{6.43(1 + 0.536U_2)D}{\lambda} \quad (1)$$

where R is the net surface radiation (converted to mm day⁻¹), A is the surface horizontal energy convergence (mm day⁻¹, ignored here), Δ is the slope vapor pressure curve (kPa °C⁻¹), γ is psychrometric constant (kPa °C⁻¹), λ is the latent heat of evaporation (MJ day⁻¹), D is surface vapor pressure deficit (kPa), U₂ is 2 m wind speed (m s⁻¹). The specific calculation of Δ , λ , γ have been described by Shuttleworth⁷⁰. Monthly data were used for these drought indices.

Data availability

All data used in this study were obtained from publicly available sources. The CMIP model outputs are distributed by the Earth System Grid Federation (ESGF) at <https://esgf-node.llnl.gov/projects/esgf-llnl/> (see Supplementary Table 1 for model details and references). Output from the CESM Last Millennium Ensemble (CESM-LME) can be downloaded at <https://www.earthsystemgrid.org/dataset/ucar.cgd.cesm4.cesmLME.html>. Reanalysis datasets are distributed by NOAA Paleo Data Search at <https://www.ncei.noaa.gov/access/paleo-search/study/24230> and <https://www.ncei.noaa.gov/access/paleo-search/study/27850>. Dai-scPDSI dataset is available at the NCAR Research Data Archive via <https://ncar.rda.dataset.ds299.0.ucar.edu>. Global-AI_PET_v3 is available at the Figshare Open Repository: https://figshare.com/articles/dataset/Global_Aridity_Index_and_Potential_Evapotranspiration_ET0_Climate_Database_v2/7504448/3.

Code availability

Codes for creating the figures and analysis were written in NCAR Command Language Version 6.5.0. and are available from the corresponding author upon a reasonable request.

Received: 1 November 2023; Accepted: 31 March 2024;

Published online: 05 April 2024

References

- Middleton, N., Thomas D. *World Atlas of Desertification*, 2nd ed. 1–181 (Oxford University, 1997).
- Huang, J. et al. Dryland climate change: Recent progress and challenges. *Rev. Geophys.* **55**, 719–778 (2017).
- Schimel, D. S. Drylands in the Earth System. *Sci* **327**, 418–419 (2010).
- Právělie, R. Drylands extent and environmental issues. A global approach. *Earth Sci. Rev.* **161**, 259–278 (2016).
- Wang, L. et al. Dryland productivity under a changing climate. *Nat. Clim. Change* **12**, 981–994 (2022).
- Huang, J., Yu, H., Guan, X., Wang, G. & Guo, R. Accelerated dryland expansion under climate change. *Nat. Clim. Change* **6**, 166–171 (2016).
- Reynolds, J. F. et al. Global Desertification: Building a Science for Dryland Development. *Science* **316**, 847–851 (2007).
- Mortimore, M. Dryland Opportunities: A new paradigm for people, ecosystems and development. <https://www.undp.org/publications/dryland-opportunities-new-paradigm-people-ecosystems-and-development> (2009).
- Grace, J., José, J. J. S., Meir, P., Miranda, H. S. & Montes, R. A. Productivity and carbon fluxes of tropical savannas. *J. Biogeogr.* **33**, 387–400 (2006).
- Wang, L. et al. Dryland ecohydrology and climate change: critical issues and technical advances. *Hydrol. Earth Syst. Sci.* **16**, 2585–2603 (2012).
- Maestre, F. T. et al. Plant Species Richness and Ecosystem Multifunctionality in Global Drylands. *Sci* **335**, 214–218 (2012).
- El-Beltagy, A. & Madkour, M. Impact of climate change on arid lands agriculture. *Agric. Food Secur.* **1**, 3 (2012).
- Huang, J. et al. An overview of the Semi-arid Climate and Environment Research Observatory over the Loess Plateau. *Adv. Atmos. Sci.* **25**, 906–921 (2008).
- Sherwood, S. & Fu, Q. A Drier Future? *Science* **343**, 737–739 (2014).
- Lian, X. et al. Multifaceted characteristics of dryland aridity changes in a warming world. *Nat. Rev. Earth Environ.* **2**, 232–250 (2021).
- Dai, A. Increasing drought under global warming in observations and models. *Nat. Clim. Change* **3**, 52–58 (2013).
- Dong, B. & Dai, A. The influence of the Interdecadal Pacific Oscillation on Temperature and Precipitation over the Globe. *Clim. Dyn.* **45**, 2667–2681 (2015).
- McCabe, G. J., Palecki, M. A. & Betancourt, J. L. Pacific and Atlantic Ocean influences on multidecadal drought frequency in the United States. *Proc. Natl Acad. Sci. USA* **101**, 4136–4141 (2004).
- Dai, A. Drought under global warming: a review. *Wiley Interdiscip. Rev. Clim. Change* **2**, 45–65 (2011a).
- Dai, A. Hydroclimatic trends during 1950–2018 over global land. *Clim. Dyn.* **56**, 4027–4049 (2021).
- Dai, A. Characteristics and trends in various forms of the Palmer Drought Severity Index during 1900–2008. *J. Geophys. Res. Atmos.* **116**, 1–26 (2011b).
- Zhu, J., Dai, A., Huang, D., Xiao, X. & Liu, Y. Subtropical drying under greenhouse gas-induced warming. *Clim. Dyn.* **61**, 4219–4242 (2023).
- Zhao, T. & Dai, A. CMIP6 Model-projected Hydroclimatic and Drought Changes and Their Causes in the 21st Century. *J. Clim.* **35**, 1–58 (2022).
- Zhao, T. & Dai, A. The Magnitude and Causes of Global Drought Changes in the Twenty-First Century under a Low–Moderate Emissions Scenario. *J. Clim.* **28**, 4490–4512 (2015).
- Cook, B. I., Smerdon, J. E., Seager, R. & Coats, S. Global warming and 21st century drying. *Clim. Dyn.* **43**, 2607–2627 (2014).
- Colose, C. M., LeGrande, A. N. & Vuille, M. Hemispherically asymmetric volcanic forcing of tropical hydroclimate during the last millennium. *Earth Syst. Dyn.* **7**, 681–696 (2016).
- Iles, C. E., Hegerl, G. C., Schurer, A. P. & Zhang, X. The effect of volcanic eruptions on global precipitation. *J. Geophys. Res. Atmos.* **118**, 8770–8786 (2013).
- Robock, A. Volcanic eruptions and climate. *Rev. Geophys.* **38**, 191–219 (2000).
- Trenberth, K. E. & Dai, A. Effects of Mount Pinatubo volcanic eruption on the hydrological cycle as an analog of geoengineering. *Geophys. Res. Lett.* **34**, L15702 (2007).
- Timmreck, C. Modeling the climatic effects of large explosive volcanic eruptions. *Adv. Rev.* **3**, 545–564 (2012).
- Bala, G., Duffy, P. B. & Taylor, K. E. Impact of geoengineering schemes on the global hydrological cycle. *Proc. Natl Acad. Sci.* **105**, 7664–7669 (2008).
- Zuo, M., Zhou, T. & Man, W. Wetter Global Arid Regions Driven by Volcanic Eruptions. *J. Geophys. Res. Atmos.* **124**, 13648–13662 (2019).
- Iles, C. E. & Hegerl, G. C. Systematic change in global patterns of streamflow following volcanic eruptions. *Nat. Geosci.* **8**, 838–842 (2015).
- Palmer, W. C. *Meteorological drought*. U.S. Weather Bureau Research Paper 45. (Department of Commerce, Washington, 1965).
- Dai, A., Trenberth, K. E. & Karl, T. R. Global variations in droughts and wet spells: 1900–1995. *Geophys. Res. Lett.* **25**, 3367–3370 (1998).

36. Dai, A., Trenberth, K. E. & Qian, T. A Global Dataset of Palmer Drought Severity Index for 1870–2002: Relationship with Soil Moisture and Effects of Surface Warming. *J. Hydrometeorol.* **5**, 1117–1130 (2004).
37. Xu, Y. et al. Climate engineering to mitigate the projected 21st-century terrestrial drying of the Americas: a direct comparison of carbon capture and sulfur injection. *Earth Syst. Dyn.* **11**, 673–695 (2020).
38. Tejedor, E., Steiger, N. J., Smerdon, J. E., Serrano-Notivol, R. & Vuille, M. Global hydroclimatic response to tropical volcanic eruptions over the last millennium. *Proc. Natl Acad. Sci.* **118**, e2019145118 (2021).
39. Stevenson, S. et al. Volcanic Eruption Signatures in the Isotope-Enabled Last Millennium Ensemble. *Paleoceanogr. Paleoclimatol* **34**, 1534–1552 (2019).
40. Chai, J. et al. A robust equatorial Pacific westerly response to tropical volcanism in multiple models. *Clim. Dyn.* **55**, 3413–3429 (2020).
41. Iles, C. E. & Hegerl, G. C. The global precipitation response to volcanic eruptions in the CMIP5 models. *Environ. Res. Lett.* **9**, 104012 (2014).
42. Feng, S. & Fu, Q. Expansion of global drylands under a warming climate. *Atmos. Chem. Phys.* **13**, 10081–10094 (2013).
43. Zhang, W. et al. Increasing precipitation variability on daily-to-multiyear time scales in a warmer world. *Sci. Adv.* **7**, eabf8021 (2021).
44. Lindzen, R. S. & Nigam, S. On the Role of Sea Surface Temperature Gradients in Forcing Low-Level Winds and Convergence in the Tropics. *J. Atmos. Sci.* **44**, 2418–2436 (1987).
45. Rodwell, M. J. & Hoskins, B. J. Monsoons and the dynamics of deserts. *Q. J. R. Meteorological Soc.* **122**, 1385–1404 (1996).
46. Wang, B., Liu, J., Kim, H.-J., Webster, P. J. & Yim, S.-Y. Recent change of the global monsoon precipitation (1979–2008). *Clim. Dyn.* **39**, 1123–1135 (2012).
47. Dogar, M. M. Impact of Tropical Volcanic Eruptions on Hadley Circulation Using a High-Resolution AGCM. *Curr. Sci.* **114**, 1284 (2018).
48. Crutzen, P. J. Albedo Enhancement by Stratospheric Sulfur Injections: A Contribution to Resolve a Policy Dilemma? *Clim. Change* **77**, 211–220 (2006).
49. Pasztor, J., Scharf, C. & Schmidt, K.-U. How to govern geoengineering? *Science* **357**, 231–231 (2017).
50. Fan, Y. et al. Solar geoengineering can alleviate climate change pressures on crop yields. *Nat. Food* **2**, 373–381 (2021).
51. Khodri, M. et al. Tropical explosive volcanic eruptions can trigger El Niño by cooling tropical Africa. *Nat. Commun.* **8**, 778 (2017).
52. Paik, S., Min, S.-K., Iles, C. E., Fischer, E. M. & Schurer, A. P. Volcanic-induced global monsoon drying modulated by diverse El Niño responses. *Sci. Adv.* **6**, eaba1212 (2020).
53. Stevenson, S., Fasullo, J. T., Otto-Bliesner, B. L., Tomas, R. A. & Gao, C. Role of eruption season in reconciling model and proxy responses to tropical volcanism. *Proc. Natl Acad. Sci.* **114**, 1822–1826 (2017).
54. Braconnot, P. et al. The Paleoclimate Modeling Intercomparison Project contribution to CMIP5. *CLIVAR Exch.* **56**, 15–19 (2011).
55. Jungclaus, J. H. et al. The PMIP4 contribution to CMIP6 – Part 3: The last millennium, scientific objective, and experimental design for the PMIP4 past1000 simulations. *Geosci. Model Dev.* **10**, 4005–4033 (2017).
56. Otto-Bliesner, B. L. et al. Climate Variability and Change since 850 CE: An Ensemble Approach with the Community Earth System Model. *Bull. Am. Meteor. Soc.* **97**, 735–754 (2016).
57. Gao, C., Robock, A. & Ammann, C. Volcanic forcing of climate over the past 1500 years: An improved ice core-based index for climate models. *J. Geophys. Res. Atmos.* **113**, D23111 (2008).
58. Crowley, T. et al. Volcanism and the Little Ice Age. *Pages Newslett.* **16**, 22–23 (2008).
59. Ammann, C. M., Joos, F., Schimel, D. S., Otto-Bliesner, B. L. & Tomas, R. A. Solar influence on climate during the past millennium: Results from transient simulations with the NCAR Climate System Model. *Proc. Natl Acad. Sci. USA* **104**, 3713–3718 (2007).
60. Toohey, M. & Sigl, M. Volcanic stratospheric sulfur injections and aerosol optical depth from 500 BCE to 1900 CE. *Earth Syst. Sci. Data* **9**, 809–831 (2017).
61. Tardif, R. et al. Last Millennium Reanalysis with an expanded proxy database and seasonal proxy modeling. *Climate* **15**, 1251–1273 (2019).
62. Steiger, N. J., Smerdon, J. E., Cook, E. R. & Cook, B. I. A reconstruction of global hydroclimate and dynamical variables over the Common Era. *Sci. Data* **5**, 180086 (2018).
63. Sigl, M. et al. Timing and climate forcing of volcanic eruptions for the past 2,500 years. *Nature* **523**, 543–549 (2015).
64. Zomer, R. J., Xu, J. & Trabucco, A. Version 3 of the Global Aridity Index and Potential Evapotranspiration Database. *Sci. Data* **9**, 409 (2022).
65. Haurwitz, M. W. & Brier, G. W. A Critique of the Superposed Epoch Analysis Method: Its Application to Solar–Weather Relations. *Mon. Weather Rev.* **109**, 2074–2079 (1981).
66. Adams, J., Mann, M. E. & Ammann, C. M. Proxy evidence for an El Niño-like response to volcanic forcing. *Nature* **426**, 274–278 (2003).
67. Wells, N., Goddard, S. & Hayes, M. J. A Self-Calibrating Palmer Drought Severity Index. *J. Clim.* **17**, 2335–2351 (2004).
68. Vicente-Serrano, S. M., Beguería, S. & López-Moreno, J. I. A Multiscalar Drought Index Sensitive to Global Warming: The Standardized Precipitation Evapotranspiration Index. *J. Clim.* **23**, 1696–1718 (2010).
69. Liu, Y., Kumar, M., Katul, G. G., Feng, X. & Konings, A. G. Plant hydraulics accentuates the effect of atmospheric moisture stress on transpiration. *Nat. Clim. Change* **10**, 691–695 (2020).
70. Shuttleworth, W. J. *Evaporation* (ed. Maidment D. R.) 125–252 (McGraw-Hill, 1993).

Acknowledgements

This study was funded by the Guangdong Major Project of Basic and Applied Basic Research (2020B0301030004) and the National Science Foundation of China (41975107, 42175061). A.D. acknowledges the support from the National Science Foundation (AGS-2015780, OISE-1743738).

Author contributions

S.Z., F.L., and A.D. conceptualized and led the work. S.Z., F.L., A.D., and T.Z. contributed to data analysis including validation and interpretation of the results. S.Z., F.L., and A.D. wrote the manuscript, and all authors reviewed and edited the manuscript.

Competing interests

The authors declare no competing interests.

Additional information

Supplementary information The online version contains supplementary material available at <https://doi.org/10.1038/s41612-024-00636-y>.

Correspondence and requests for materials should be addressed to Fei Liu or Aiguo Dai.

Reprints and permissions information is available at <http://www.nature.com/reprints>

Publisher's note Springer Nature remains neutral with regard to jurisdictional claims in published maps and institutional affiliations.

Open Access This article is licensed under a Creative Commons Attribution 4.0 International License, which permits use, sharing, adaptation, distribution and reproduction in any medium or format, as long as you give appropriate credit to the original author(s) and the source, provide a link to the Creative Commons licence, and indicate if changes were made. The images or other third party material in this article are included in the article's Creative Commons licence, unless indicated otherwise in a credit line to the material. If material is not included in the article's Creative Commons licence and your intended use is not permitted by statutory regulation or exceeds the permitted use, you will need to obtain permission directly from the copyright holder. To view a copy of this licence, visit <http://creativecommons.org/licenses/by/4.0/>.

© The Author(s) 2024